Check for updates

Lead-free 2D MASnBr₃ and Ruddlesden–Popper BA₂MASn₂Br₇ as light harvesting materials†

Sandip R. Kumavat and Yogesh Sonvane ⓘ *

We have explored the structural, electronic, charge transport, and optical properties of lead-free 2D hybrid halide perovskites, MASnBr₃ and Ruddlesden–Popper perovskites, BAMASn₂Br₇ monolayers. Under density functional theory (DFT) calculation, we applied mechanical strain, *i.e.*, tensile and compressive strain up to 10% in both cases. The mechanical strain engineering technique is useful for a tuned bandgap of 2D MASnBr₃ and 2D BAMASn₂Br₇. The calculated carrier mobility for the electron is 404 cm² V⁻¹ s⁻¹ and for the hole is up to 800 cm² V⁻¹ s⁻¹ for MASnBr₃. For BAMASn₂Br₇ the highest carrier mobility is up to 557 cm² V⁻¹ s⁻¹ for electrons and up to 779 cm² V⁻¹ s⁻¹ for the hole, which is 14% and 24% higher than the reported lead-iodide based perovskites, respectively. The calculated solar cell efficiency of 2D MASnBr₃ is 23.46%, which is 18% higher than the reported lead-based perovskites. Furthermore, the optical activity of the 2D MASnBr₃ and 2D BAMASn₂Br₇ shows a high static dielectric constant of 2.48 and 2.14, respectively. This is useful to show nanodevice performance. Also, 2D MASNBr₃ shows a high absorption coefficient of 15.25 × 10⁵ cm⁻¹ and 2D BAMASn₂Br₇ shows an absorption coefficient of up to 13.38 × 10⁵ cm⁻¹. Therefore our theoretical results suggest that the systems are under mechanical strain engineering. This is convenient for experimentalists to improve the performance of the 2D perovskites. The study supports these materials as good candidates for photovoltaic and optoelectronic device applications.

1. Introduction

Nowadays, energy crises and environmental pollution are the main big problems for humans. Many research groups are working on finding alternative solutions for these problems. Globally, educational and industrial purpose scientific communities are now attracted to renewable energy sources, and have developed new technology to overcome such situations and find low-cost solutions. The research community has recently become interested in organic–inorganic hybrid halide perovskites because of their rapid advancement in photovoltaics and optoelectronics over the past ten years.[1] Compared with traditional silicon cells, these hybrid halide perovskites solar cells reached a power conversion efficiency (PCE) of more than 24% within a few years.[1–4] Their electronic properties include a high extinction coefficient, tunable bandgaps, long carrier mobility, and a long charge transport diffusion path.[5–8] However, with these advantages, chemical instability is the central issue. These hybrid halide perovskites being highly reactive with moisture is the main drawback for industrial purposes.[9–12]

Many technologies have developed and extracted the two-dimensional 2D slab by slicing from the 3D framework of hybrid halide perovskites.[13–15] The transformation of 3D to 2D perovskite opens the potential to more clearly analyze electronic, optical, and transport properties.[16] These 2D hybrid halide perovskites are a stable candidate for optoelectronic devices. Like light-emitting diodes,[17] photocatalysts, field-effect transistors,[17–19] lasers, *etc.*[20–25] Also, these 2D perovskites have flexible structural and compositional properties. Long-term stability characteristics in ambient conditions, more moisture resistance than 3D structure, and tunable photovoltaic properties.[26–30] 2D third-generation hybrid halide perovskites have the structural formula MAZX₃ (ref. 31–34) (MA = CH₃NH₃, Z = Pb, Sn and X = Cl, Br, I). These 2D perovskites interact well with inorganic layers, same as Ruddlesden–Popper 2D structures,[35–40] which has structural formula (BA)₂MAZ₂X₇ (BA = CH₃(CH₂)₃NH₃, MA = CH₃NH₃, Z = Pb, Sn, X = Cl, Br, I). Due to the structural flexibility of 2D perovskites, many groups have developed a new technique to find its efficient power conversion efficiency (PCE). 2D material interfacing with 2D perovskites has reached PCE 12.6%.[12,15,41] 2D lead halide CH₃NH₃PbI₃ and Ruddlesden–Popper (CH₃(CH₂)₃NH₃)₂CH₃NH₃Pb₂I₇ have reached 14.9%, 17%, and 19.7% PCE in theoretical experiments, respectively.[42–44] Yang *et al.*'s group reached 20% PCE by interfacing 2D with 3D perovskites.[45] Under condition Shockley–Queisser limit, PCE of perovskites was achieved 31% with

Advanced Materials Lab, Department of Physics, Sardar Vallabhbhai National Institute of Technology, Surat 395007, India. E-mail: yas@phy.svnit.ac.in

the theoretical study.[46] The 2D lead (Pb) hybrid halide perovskites have been considered good candidates as light-harvesting materials. But has toxicity issues with environmental effects.[47] To solve the problem of environmentally and humanly hazardous hybrid halide perovskites based on lead (Pb). Researchers have discovered that substituting alternative divalent elements, such as In, Sn, Sb, Bi, *etc.*, for lead is advantageous for both the environment and human beings. Experimentally, the tin (Sn) based halide perovskites are isostructural compounds of Pb-based halide.[31] Sn-based halide perovskites materials contain a narrow optical bandgap high optical absorption coefficient. Also, it contains high charge carrier mobility with low exiting binding energy and good stability.[48–50] Experimentally, the tin-based halide materials work as a light-harvesting material covering a wide range of visible spectrums. Furthermore, we have found that many groups are working on lead-free tin-based hybrid halide perovskites. The Xu *et al.* group is tuning the optical band gap of perovskites for light harvester materials.[51] For thermoelectric devices, these materials were used.[52] Ruddlesden–Popper nonlinear band behaviour due to mismatch s-states of Pb and Sn design a metal alloy.[36] As the number of 2D layers increases band, behaviour shows charge carries effect well compared with experimental result.[53] Therefore, these studies are useful for developing new building blocks for future photovoltaic and optoelectronic devices.[54–62]

In this paper, we give a comparative analysis of two orthorhombic structures of hybrid halide perovskites using density functional theory (DFT) calculations. $CH_3NH_3SnBr_3$ as ($MASnBr_3$) (MA = CH_3NH_3) and Ruddlesden–Popper $(CH_3(CH_2)_3NH_3)_2CH_3NH_3Sn_2Br_7$ as ($BAMASn_2Br_7$) (BA = $(CH_3(CH_2)_3NH_3)_2$, MA = CH_3NH_3) perovskites with their structural, electronic, optical and transport properties. Under mechanical strain conditions, we apply both tensile and compressive strain up to 10%. Mechanical strain condition is a valuable way to tune the electronic and optical properties of 2D halide perovskites because of the flexible structural and composition properties. For the creation of lead-free 2D hybrid halide perovskites for optoelectronic and photovoltaic

applications, mechanical strain engineering offers a novel route.

2. Methodology

Density functional theory (DFT) and the Vienna *ab initio* simulation package (VASP) are used for all structural and electrical calculations.[63–66] The projected augmented wave (PAW) method used the generalized gradient approximation (GGA) exchange–correlation Perdew–Burke–Ernzerhof (PBE) functional.[66] The van der Waals (vdW) is included in our calculations. We also include SOC and HSE calculation to find more clear results.[67] The plane-wave kinetic energy cut-off is set to 500 eV. The Brillouin zone (BZ) *k*-point grid ($5 \times 5 \times 1$) was used for structure optimisation. Also ($15 \times 15 \times 1$) *k*-point grid was selected for further electronic properties. All atomic structures of $MASnBr_3$ (MA = CH_3NH_3) and Ruddlesden–Popper $(BA)_2$-$MASn_2Br_7$ (BA = $CH_3(CH_2)_3NH_3$, MA = CH_3NH_3) are converged up to the force 0.0001 eV Å^{-1} and total energy at 10^{-4} eV. To define structural balance, we used the ionic radii based tolerance factor formula $t = (R_A + R_X)/\sqrt{2}(R_B + R_X)$ should be in the range between 0.813 and 1.107.[5] Optical properties can be estimated through the Kramers–Kronig transformation based on the electronic structure.[68–71] The optical absorption coefficient can be calculated using the formula:

$$\alpha(\omega) = \sqrt{2}\omega\left(\left[\varepsilon_1{}^2 + \varepsilon_2{}^2\right]^2 - \varepsilon_1\right)^{1/2} \tag{1}$$

3. Results and discussions

3.1 Structural and electronic properties

Here, we have studied the structural parameter of hybrid halide $MASnBr_3$ and $BAMASn_2Br_7$ monolayer, as shown in Fig. 1(a) and 2(a). The lattice parameters exhibit good agreement with those that have been previously reported, as shown in Table 1. We have not found much research on $BAMASn_2Br_7$ monolayers during the literature survey. Here we replaced lead (Pb) with tin (Sn),[41,43] which has an ionic radius smaller than Pb and the ionic
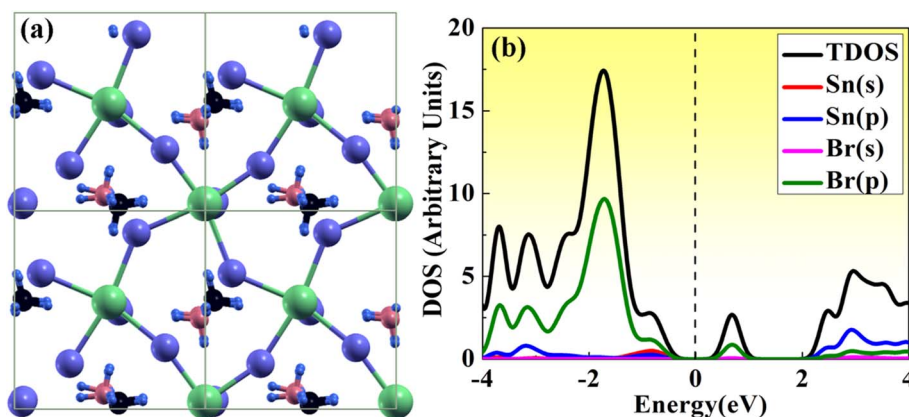

Fig. 1 (a) Atomic structure of $MASnBr_3$, where Sn, Br, C, N, H atom are represented in green, violet, black, dark pink, sky blue respectively. (b) Calculated total (TDOS) and projected density of states (PDOS) of $MASnBr_3$.
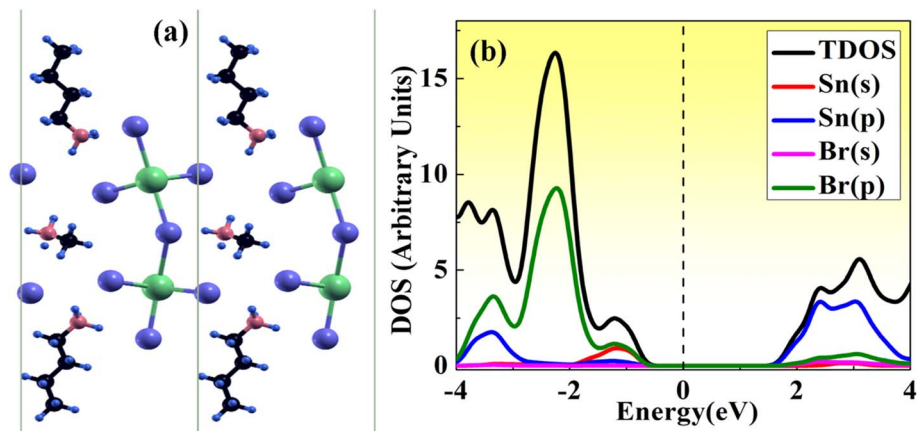
Fig. 2 (a) Atomic structure of BAMASn₂Br₇, where Sn, Br, C, N, H atom are represented in green, violet, black, dark pink, sky blue respectively. (b) Calculated total (TDOS) and projected density of states (PDOS) of BAMASn₂Br₇.

Table 1 Calculated lattice parameter of MASnBr₃ and BAMASn₂Br₇ monolayer

	a (Å)	b (Å)	Other
MASnBr₃	8.08	8.5	8.5 (ref. 54 and 55)
BAMASn₂Br₇	7.20	5.21	6.0 (ref. 57)

radius of halogen iodide (I) replaced by bromine (Br). The corresponding lattice parameters are of the 2D MASnBr₃, and BAMASn₂Br₇ monolayer smaller respectively as lead based 2D perovskites.[10,41,43]

With all these replacements, Sn and Br perovskites structure becomes more stable and does not have much change in the structural phase. Also, for both structures corresponding
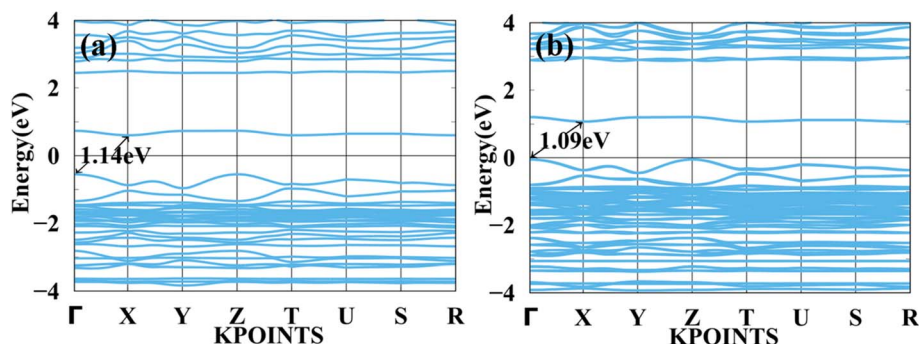

Fig. 3 Calculated band structure of MASnBr₃ with (a) PBE and (b) spin orbit coupling (SOC) represented.
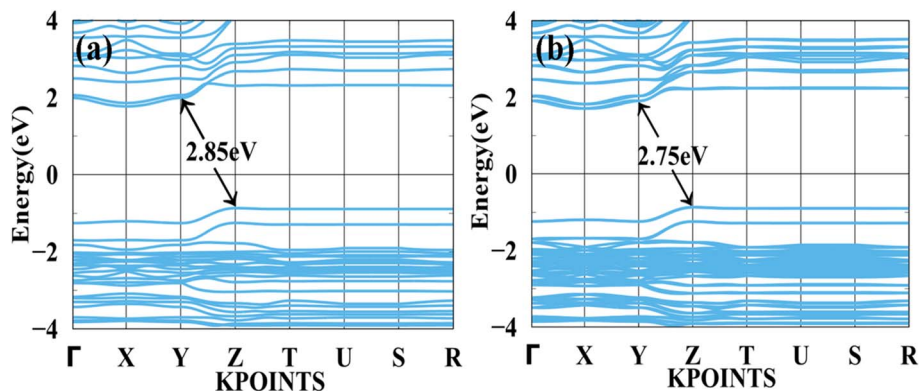

Fig. 4 Calculated band structure of BAMASn₂Br₇ with (a) PBE and (b) spin orbit coupling (SOC) represented.

tolerance factor is in the range of 0.8 < t < 1.0, with consistence formation energy 141 eV for MASnBr$_3$ and 196 eV for BAMASn$_2$Br$_7$.

Furthermore, we have calculated the total density of states (TDOS) and projected density of states (PDOS) of MASnBr$_3$ and BAMASn$_2$Br$_7$ in Fig. 1(b) and 2(b). In Fig. 1(b) it is clearly seen that in the valence band of MASnBr$_3$, most of the part is contributed with the Br-p states with Sn-s states. While in the conduction band, most of the part is covered by the Sn-p states. Similarly, in the case of the Ruddlesden–Popper BAMASn$_2$Br$_7$ perovskites, most of the part valence band is contributed with

the Sn-s and Br-p states. The conduction band is coved with the Sn-p states as shown in Fig. 2(b). Also, in both systems, null contributions of organic molecules in valence and conduction bands are observed. In Fig. 3 and 4 shows the calculated band structure of the MASnBr$_3$ and BAMASn$_2$Br$_7$. Fig. 3(a) contain the band structure of MASnBr$_3$ with PBE (without SOC) and Fig. 3(b) with SOC. The calculated indirect bandgap is along with gamma to x point 1.14 eV. Which is consistent with previously reported results.[52]

In Fig. 4(a) shows a bandgap of BAMASn$_2$Br$_7$ PBE (without SOC) and Fig. 4(b) with SOC. Here, the case of Ruddlesden–
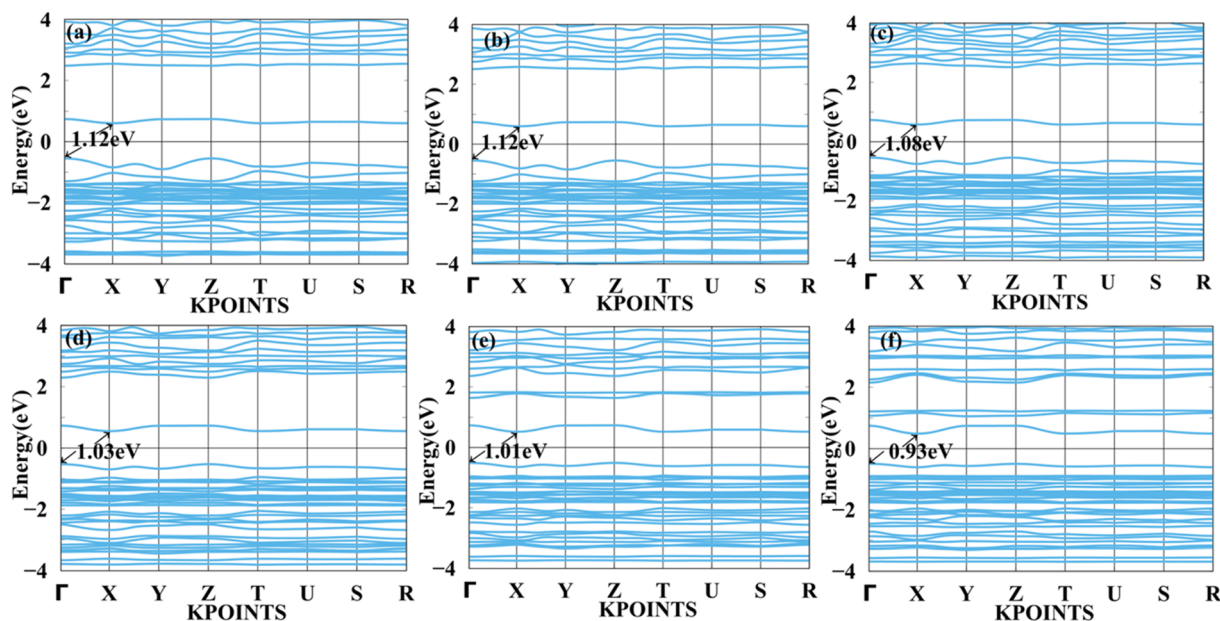

Fig. 5 Calculated tensile strain band structure of MASnBr$_3$ with (a) 1%, (b) 2%, (c) 4%, (d) 6%, (e) 8% and (f) 10% respectively.
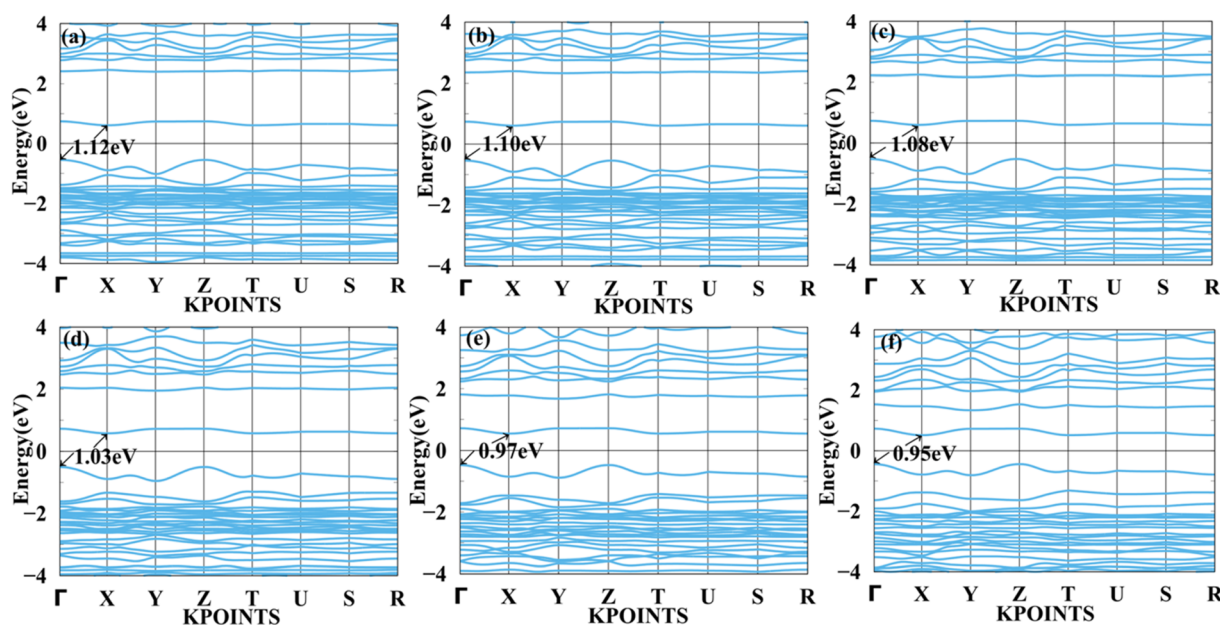

Fig. 6 Calculated compressive strain band structure of MASnBr$_3$ with (a) 1%, (b) 2%, (c) 4%, (d) 6%, (e) 8% and (f) 10% respectively.
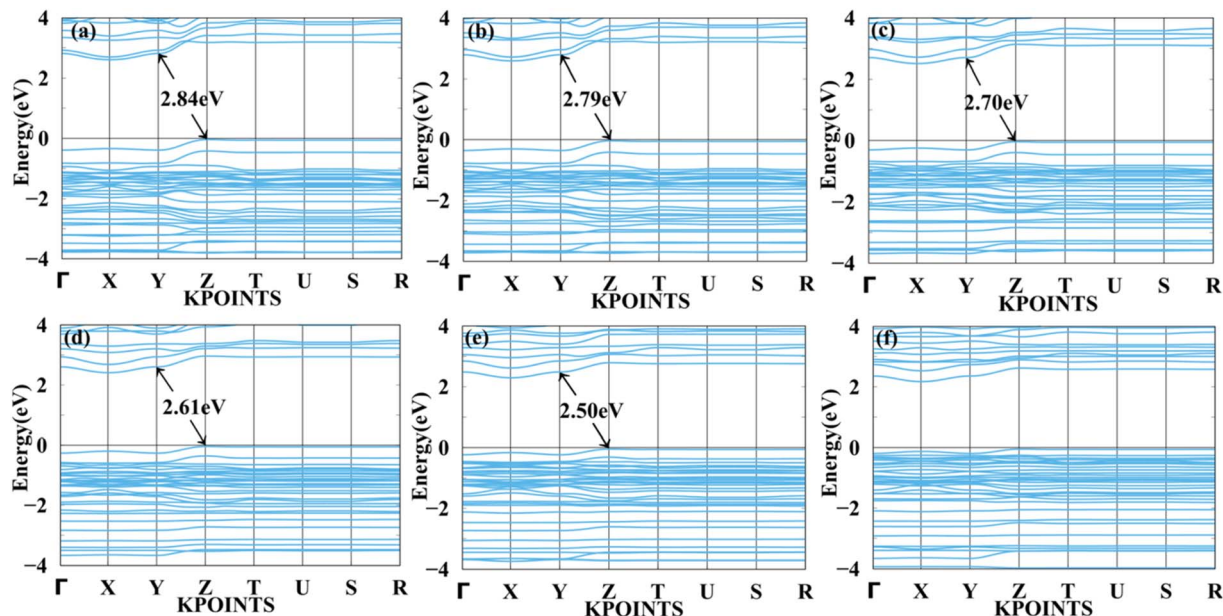
Fig. 7   Calculated tensile strain band structure of BAMASn$_2$Br$_7$ with (a) 1%, (b) 2%, (c) 4%, (d) 6%, (e) 8% and (f) 10% respectively.

Popper perovskite BAMASn$_2$Br$_7$ indirect bandgap is at Z to Y point 2.85 eV. BAMASn$_2$Br$_7$ perovskites have not been much studied, but compared with related Ruddlesden–Popper are like BAMASn$_2$I$_7$ consistent.[36,43,58,59] Also, when we replace Pb with Sn and iodine by Br, corresponding lattice parameters decrease with increasing corresponding band gaps.[41] In both cases, we have seen that under the SOC study, there is not much effective change in indirect bandgap observed.[5,41,43] An orbital contribution point of view in valence band maxima (VBM) is mostly contributed by the Sn-5s and Br-4p orbitals. While conduction band minima, most of the part is contributed with the Sn-5p and 4 s, 4p orbitals of Br atom.

3.2   Strain engineering

We applied mechanical strain to both systems to moderate electronic properties as shown in Fig. 5 and 6 for MASnBr$_3$, Fig. 7 and 8 for BAMASn$_2$Br$_7$. Due to flexible structural and compositional properties, mechanical strain is an efficient way to tune electronic properties.[5,41] As per literature survey, we found that there are many experimental as well as theoretical techniques have been developed to improve only performance of the system or device. In the literature survey we found that there are no other studies on strain dependent on 2D MASnBr$_3$ and Ruddlesden–Popper BA$_2$MASn$_2$Br$_7$ orthorhombic
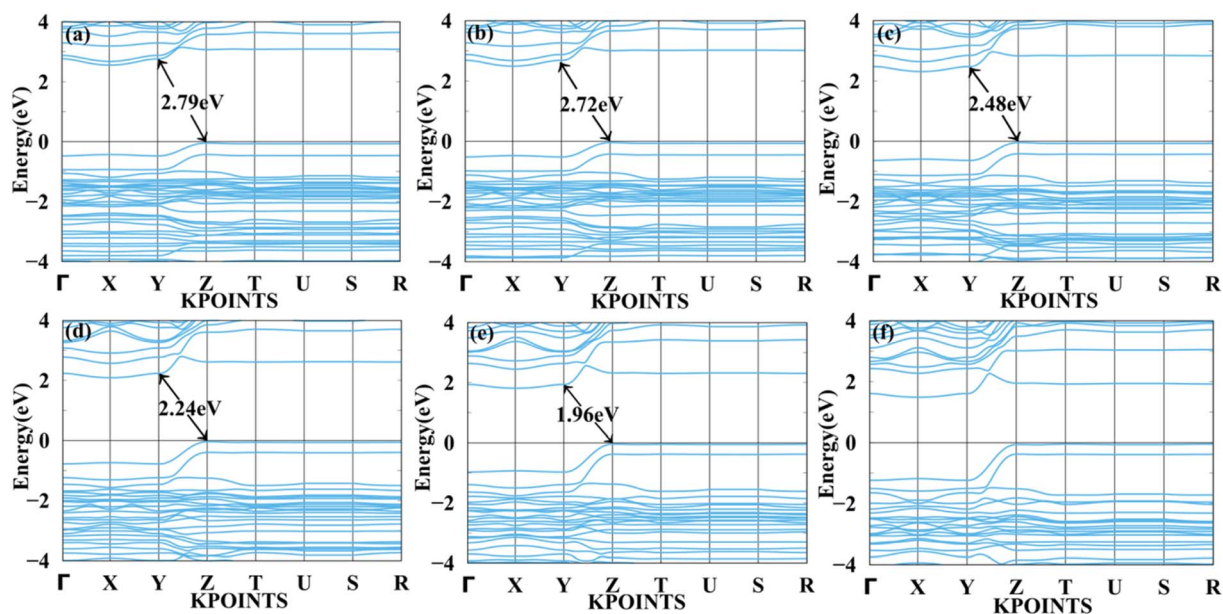

Fig. 8   Calculated compressive strain band structure of BAMASn$_2$Br$_7$ with (a) 1%, (b) 2%, (c) 4%, (d) 6%, (e) 8% and (f) 10% respectively.
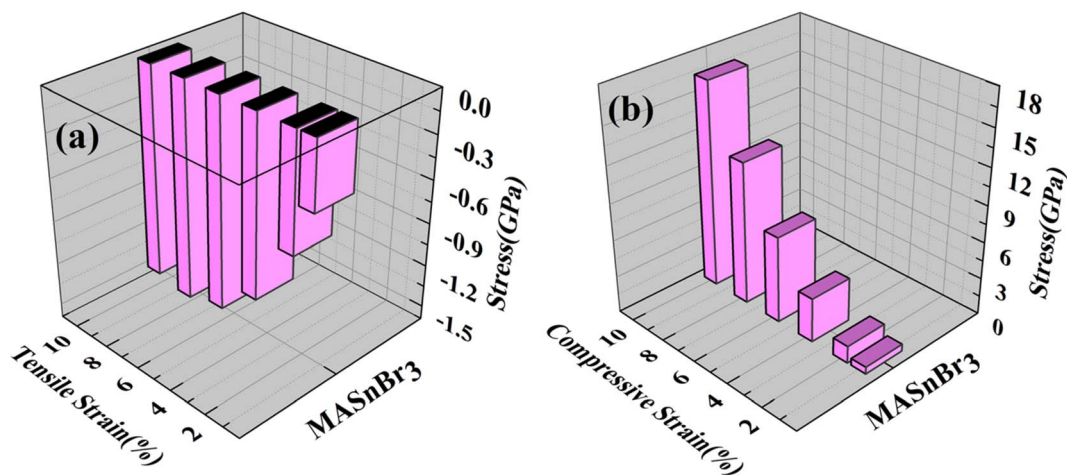
Fig. 9 Applied (a) tensile and (b) compressive strain *versus* stress for the MASnBr$_3$.

structures. Lattice strain is promising technique to improve performance of the many 2D materials. This has been useful for both experimental as well as theoretical groups. As per experimental researches studies of hetero epitaxial perovskite thin films shows that lattice strain play an important role to determining the physical properties of the thin films.[5,41,60,61] In the case of the MASnBr$_3$ system, we have applied both tensile and compressive strain along the x and y directions from 1% to 10% in the interval of 2%. Under tensile strain, condition bandgap was consistently decreased from 1% to 10% from 1.12 eV to 0.93 eV, as shown in Fig. 5. Similarly, compressive strain band gap decreases consistently 1% to 10% from 1.12 eV to 0.95 eV as shown in Fig. 6. Compared with the unstrained system with both tensile and compressive strain systems, the bandgap was decreased because the valence band contains most of the part of antibonding states of Br-p and Sn-s orbitals. In comparison, the conduction band contains most of the non-antibonding states of Br-p and Sn-p orbitals. Therefore near the Fermi level,

downward shifting of conduction bands and upward shifting of valence band occurred effectively.

Fig. 7 and 8 show the tensile and compressive strain-dependent band structure of BAMASn$_2$Br$_7$ perovskites. Here, under conditions of tensile strain, bandgap reduces as strain is increased by 1%, 2%, 4%, 6%, or 8%, going from 2.84 eV to 2.792 eV to 2.70 eV to 2.61 eV to 2.50 eV. Similarly, in compressive strain conditions, band gaps decrease from 1% to 8% to 2.84 eV to 1.96 eV. At 10% both types of strain show metallic behaviour. That means the sustainability of the structure is up to 8%. Further, in Ruddlesden–Popper BAMASn$_2$Br$_7$. Comparison between the unstrained systems with strain systems of nature of the bandgap varies. Due to the presence of antibonding states of Br-p and Sn-s orbitals in valence bands. Non-antibonding states of Br-p and Sn-p orbital's in conduction bands are similar as that of the MASnBr$_3$ perovskites. Overall, the mechanical strain technique is useful for tuning the bandgap and open the path for experimentalists to study thin films' physical and chemical properties.[5,60]
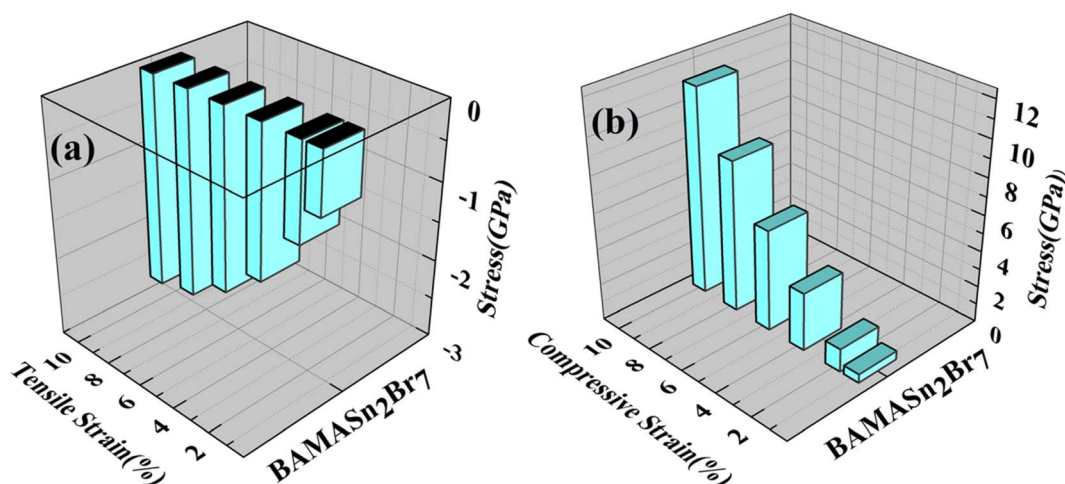

**Fig. 10** Applied (a) tensile and (b) compressive strain *versus* stress to the BAMASn$_2$Br$_7$.

Table 2 Calculated effective mass, carrier mobility, and relaxation time of MASnBr$_3$ and BAMASn$_2$Br$_7$ respectively

System		m_e^* (m_0)	m_h^* (m_0)	C (N m^{-1})	μ_e (cm^2 V^{-1} s^{-1})	μ_h (cm^2 V^{-1} s^{-1})	τ_e (fs)	τ_h (fs)
MASnBr$_3$	X	0.122	0.0578	19.17	248.0	181.6	30.25	10.49
	Y	0.361	0.0633	19.17	404.2	800	146	50.64
BAMASn$_2$Br$_7$	X	0.160	0.336	7.97	557	124.1	89.34	41.69
	Z	0.146	0.320	7.97	367.4	779	53.64	249

Using the Hellmann–Feynman theorem[61] In Fig. 9 and 10 we have calculated stress on both systems. In both cases, we applied strain on the overall system along the x-axis and y-axis for MASnBr$_3$ x-axis and z-axis for BAMASn$_2$Br$_7$. Overall stress was increased from 1% to 10%. Compared with tensile and compressive strain, in both systems, compressive stress is more and tensile stress is less. This change is happened due to contractions and expansion of lattice parameters of the system as shown in 2D barplot in Fig. S1.† Which effect the inter-bonding activity of the atoms. In the case of the MASnBr$_3$ system, the structure's sustainability is up to 10% in both tensile and compressive. While in the case of BAMASn$_2$Br$_7$, the sustainability of the strain is up to 8%. After that, both systems show metallic nature.

3.3 Charge carrier mobility

Further, we have a focus on the charge transport properties of both systems. Due to flexible structural and compositional properties, these systems are well sustained in strain conditions, bands experience a high degree of dispersion and have a bandgap near optical band gaps.[51] Near the Fermi level, the directional dependent effective mass of both electrons and holes with the slope of x, y, z-axis direction are shown in Table 2. The effective mass of the electron and holes for MASnBr$_3$ along x and y directions are 0.36 to 0.057 and for Ruddlesden–Popper BAMASn$_2$Br$_7$ along x and z-direction are 0.33 to 0.146. In both cases, the effective mass of electrons and holes is remarkably more than the previously reported.[35,43,62]
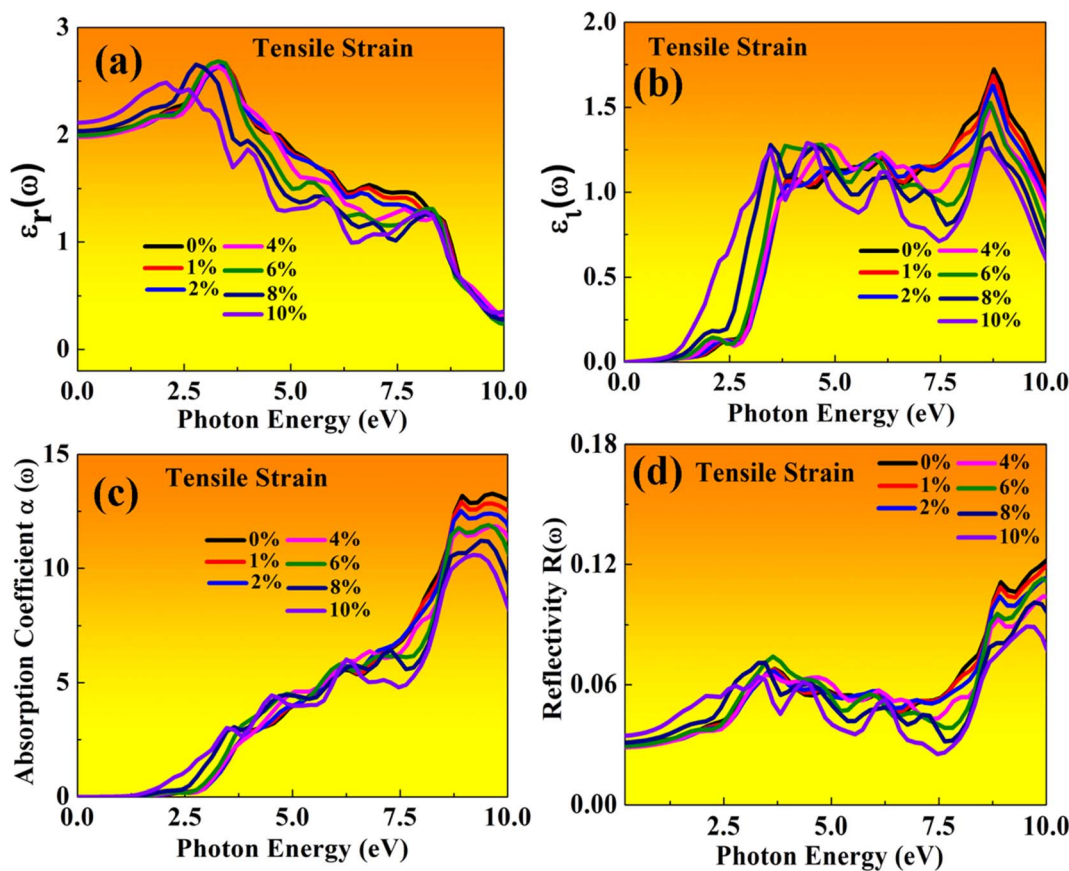
Fig. 11 Optical properties of MASnBr$_3$ perovskites represented with tensile strain: (a) real $\varepsilon_r(\omega)$, (b) imaginary $\varepsilon_i(\omega)$, (c) absorption coefficient, (d) reflectivity.
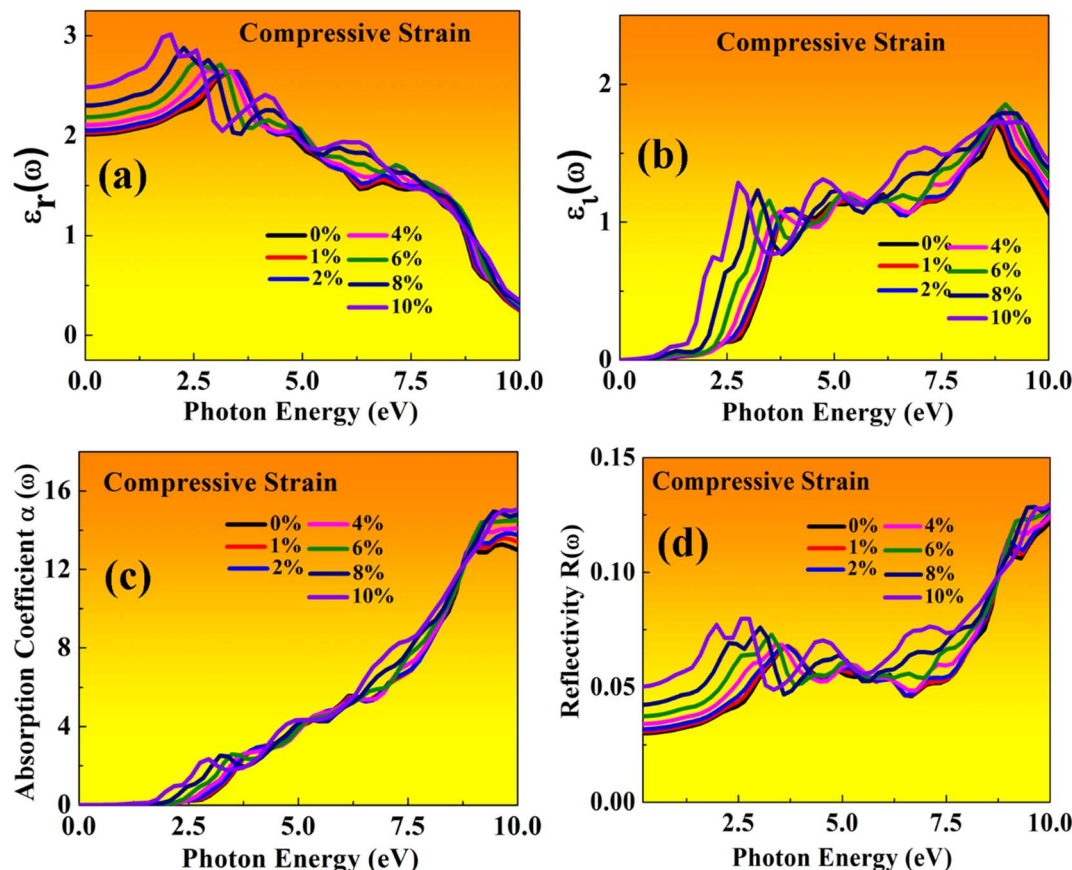
Fig. 12 Optical properties of MASnBr$_3$ perovskites represented with compressive strain: (a) real $\varepsilon_r(\omega)$, (b) imaginary $\varepsilon_i(\omega)$, (c) absorption coefficient, (d) reflectivity.

We also calculate the charge transport carrier mobility and relaxation time using deformation potential theory. Which leads to calculate using formula

$$\mu_x = \frac{eh^3 C_x}{(2\pi)^3 k_B T m_x^* m_d E_{1x}^2} \tag{2}$$

Also carrier mobility dependent relaxation time (τ), $\tau = (\mu m^*)/e$ as shown in Table 2. Here e stand for electron charge, h for Planck's constant, m^* for effective mass $m_d = (\sqrt{m_x^* m_y^*})$, $E_{1x} = \Delta V/(\Delta a_x/a_x)$ deformation potentials.[5] In the case of MASnBr$_3$, the calculated carrier mobility of holes is higher than the electrons. Similar trends were observed in BAMASn$_2$Br$_7$, the hole carrier mobility is higher than the electrons. In compared with lead-iodide-based perovskites, carrier mobility of Sn-bromide-based perovskite is 14% and 24% higher, which are quite larger than the reported experimental and theoretical data.[5,35,41,43,62] This anisotropic nature of carrier mobility is due to smaller effective mass and flexible structural properties, affecting the band gaps. This high carrier mobility leads to better device performance. Open a new path for experimentalists to find solar cell efficiency and developed optoelectronic devices.

3.4 Optical properties

Here, both perovskites structures have flexible electronic and structural properties, which is useful for determining their optical behaviour in both tensile and compressive strains. Using frequency-dependent Kramer–Kronig relation developed by Drude model.[70,71] We are focused on optical properties in Fig. 11 and 12 shown in MASnBr$_3$ under tensile and compressive strains, while in Fig. 13 and 14 shows optical properties of BAMASn$_2$Br$_7$ under mechanical strain conditions.

In the real part of the MASnBr$_3$, the static dielectric constant is 2.011. Further, increases in tensile strain the static dielectric constant from 1.99 to 2.11. In compressive strain from 2.02 to 2.48 for 1% to 10%, as shown in Fig. 11(a) and 12(a), respectively. In the case Ruddlesden–Popper BAMASn$_2$Br$_7$ optical properties, the real part static dielectric constant is 2.01. Under mechanical strain conditions, the static dielectric constant decreases in tensile strain from 2.01 to 1.98 from 1% to 10%, while in the case of compressive strain static dielectric constant are increases from 1.9 to 2.14 from 1% to 10% as shown in Fig. 13(a) and 14(a) respectively. These high values of static dielectric constant are useful to define optoelectronic device performance. Similarly, in both cases, the imaginary part of static dielectric constant the optical activity is due to the
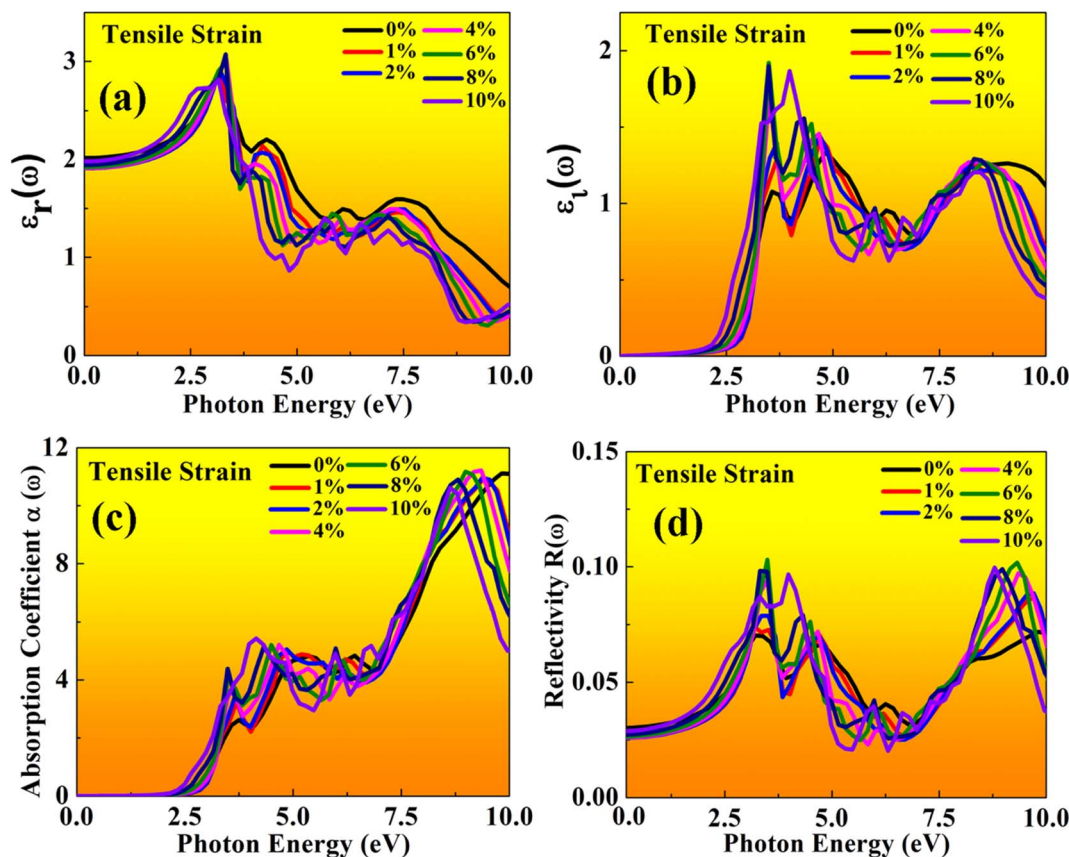
Fig. 13 Optical properties of BAMASn$_2$Br$_7$ perovskites represented with tensile strain: (a) real $\varepsilon_r(\omega)$, (b) imaginary $\varepsilon_i(\omega)$, (c) absorption coefficient, (d) reflectivity.

transition of the electron in valence band Sn-s states to Br-p states in the conduction band.

In both cases, the first peak is at 2.5 eV. After applying both tensile and compressive strain, optical activity orientation is a move towards high energy part 8 eV as shown in Fig. 11(b) and 12(b) for MASnBr$_3$, Fig. 13(b), 14(b) for BAMASn$_2$Br$_7$. Further, optical properties are analyzed by absorption coefficient, reflectivity. In the case of MASnBr$_3$ absorption coefficient is at 13.27×10^5 cm^{-1} at 8.8 eV. Which are further decreases from 12.91×10^5 cm^{-1} to 10.58×10^5 cm^{-1} in tensile strain from 1% to 10% as shown in Fig. 11(c). In case compressive strain absorption coefficient increases from 13.60×10^5 cm^{-1} to 15.25×10^5 cm^{-1} for 1% to 10% as shown in Fig. 12(c). Also, in the case of BAMASn$_2$Br$_7$ absorption coefficient is 11.11×10^5 cm^{-1} for the unstrained system. For tensile strain it is decreases from 10.91×10^5 cm^{-1} to 10.62×10^5 cm^{-1} for 1% to 10% as shown in Fig. 13(c) and in case of compressive strain it is increases from 11.14×10^5 cm^{-1} to 13.38×10^5 cm^{-1} for 1% to 10% as shown in Fig. 14(c). The first small peak orientation is near 2.5 eV, which shows optical band gap activity is in the range of previously reported data.[33,35,47] Overall, the optical activity of MASnBr$_3$ and BAMASn$_2$Br$_7$ are shown. By reflectivity by the orientation of peaks at 0 eV to 2.5 eV and 2.5 eV to 5 eV, and further 10 eV is in the visible (500–414 nm) as well as ultraviolet region(310–177 nm) of the energy spectrum as shown if

Fig. 11(d), 12(d), 13(d) and 14(d). Therefore maximum light reflects in the visible as well as in the ultraviolet region. These studies are consistent with the previously reported experimental and theoretical studies.[33,35,47] Overall, compared with MASnBr$_3$ and BAMASn$_2$Br$_7$ perovskites with other 2D hybrid halide perovskites. Tunable band gap and optical, charge transport activity useful for photovoltaic and solar cell devices.

3.5 Solar cell efficiency parameter

Further, we have investigated the solar cell efficiency performance of 2D MASnBr$_3$. The Shockley and Queisser (SQ) model depend on the material's bandgap. To calculate the performance of solar cell efficiency, the band gap are required to be in between 1.0 to 1.7 eV. Therefore, the bandgap of 2D MASnBr$_3$ is under SQ limit and band gap of BAMASn$_2$Br$_7$ are higher than the SQ limit. The solar cell parameters like open-circuit voltage (V_{oc}), fill factor (FF), short circuit current density (J_{sc}), and solar cell efficiency are calculated as per previously reported results.[5,41] More information is provided in the ESI† as shown in Tables 3, S1 and S2.†

For 2D MASnBr$_3$ solar cell efficiency is 23.46%. Which is 18% larger than that of the previously reported lead-based 2D MAPbI$_3$ (ref. 43) perovskites. Also, we have found that in comparison with experimental results. The power conversion efficiency of lead-
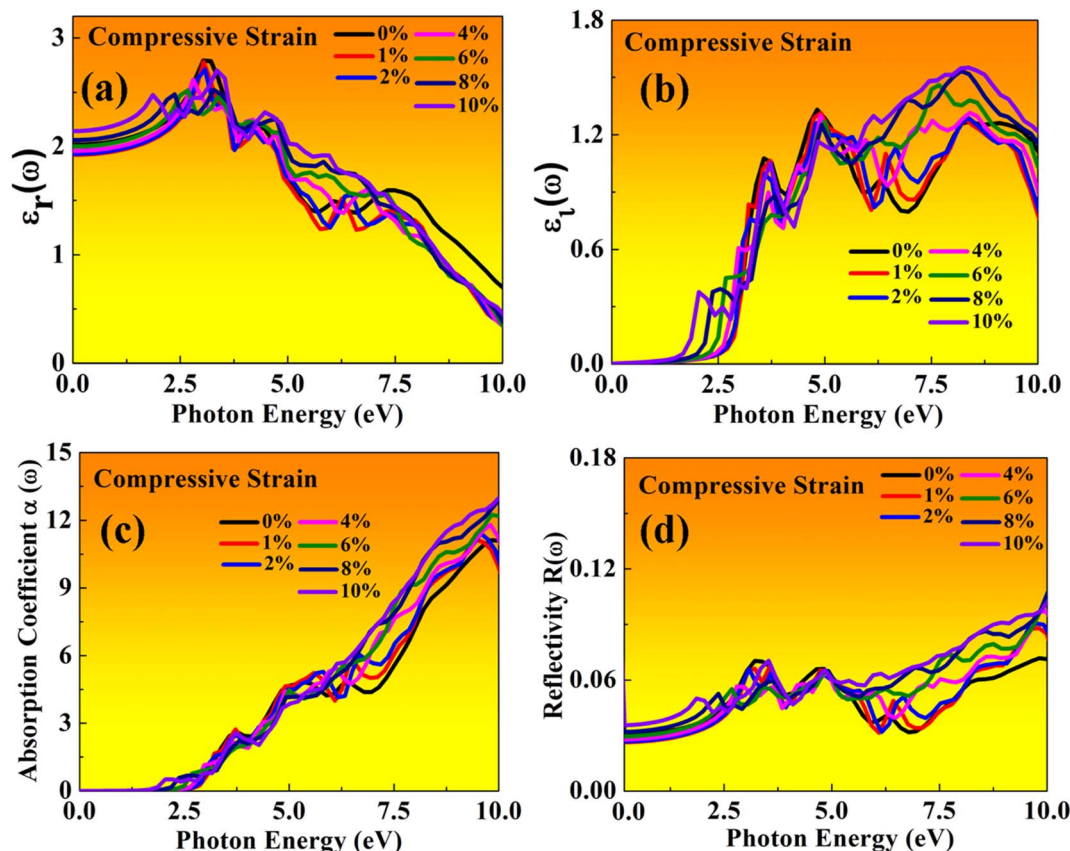
Fig. 14 Optical properties of $BAMASn_2Br_7$ perovskites represented with compressive strain: (a) real $\varepsilon_r(\omega)$, (b) imaginary $\varepsilon_i(\omega)$, (c) absorption coefficient, (d) reflectivity.

Table 3 Represents calculated solar cell parameters for open circuit voltage, fill factor, short circuit current density, power conversion efficiency of $MASnBr_3$ monolayer

	V_{oc} (eV)	FF	J_{sc} (mA cm^{-2})	H (%)
$MASnBr_3$	2.64	0.94	9.40	23.46

free perovskites developed by Hao *et al.* and Xu *et al.* group have reached up to 5.73% and 8.79%, respectively.[49,51] Overall in comparison with lead-free 3D hybrid halide perovskites with 2D hybrid halide perovskites. The 2D hybrid halide perovskites are more efficient and suitable candidates to develop new generation solar cells.[5,41,43,49,51,57] Under both tensile and compressive strain conditions. The calculated solar cell efficiency varies from 13% to 23% as shown in Tables 3, S1 and S2.† Therefore we conclude that the lead-free 2D $MASnBr_3$ is a suitable candidate for solar cell and photovoltaic applications.

4. Conclusions

Here, the 2D $MASnBr_3$ and Ruddlesden–Popper perovskites $BAMASn_2Br_7$ hybrid halide perovskites have flexible structural and compositional properties. Also, the calculated bandgap and lattice parameters of $MASnBr_3$ and Ruddlesden–Popper perovskites $BAMASn_2Br_7$ are consistent with previously reported experimental and theoretical results. Under mechanical strain, *i.e.*, tensile and compressive strain tunable bandgap activity is consistent with previously reported, showing sustainability of the structure up 10% in $MASnBr_3$ and up to 8% in $BAMASn_2Br_7$. We found highest carrier mobility for electron up to 404 cm^2 V^{-1} s^{-1} and holes 800 cm^2 V^{-1} s^{-1} for $MASnBr_3$, and $BAMASn_2Br_7$ highest carrier mobility up to 557 cm^2 V^{-1} s^{-1} for electron and up to 779 cm^2 V^{-1} s^{-1} for the hole, which are 14% and 24% higher than the reported data. The calculated solar cell parameters open-circuit voltage (V_{oc}), fill factor (FF), short circuit current density (J_{sc}), and solar cell efficiency are consistent with the previously reported experimental and theoretical results. Here, tin-based 2D $MASnBr_3$ shows high efficiency up to 23.46%, 18% higher than the lead-based perovskites. In optical activity, a high static dielectric constant shows good device performance. With high absorption coefficient up to 15.25 × 10^5 cm^{-1} for $MASnBr_3$ and $BAMASn_2Br_7$ absorption coefficient up to 13.38 × 10^5 cm^{-1}. Therefore overall results of this theoretical study. With mechanical strain engineering may be convenient to the experimentalist support to improve the performance of the 2D perovskites. This study supports these materials as promising candidates for photovoltaic and solar cell device applications.

Conflicts of interest

There are no conflicts to declare.

Acknowledgements

References

1 C. Liu, W. Ding, X. Zhou, J. Gao, C. Cheng, X. Zhao and B. Xu, Efficient and Stable Perovskite Solar Cells Prepared in Ambient Air Based on Surface-Modified Perovskite Layer, *J. Phys. Chem. C*, 2017, **121**, 6546–6553.

2 G. Grancini, C. Roldan-Carmona, I. Zimmermann, E. Masconi, X. Lee, D. Martineau, S. Narbey, F. Oswald, F. D. Angelis, M. Gratzel and M. K. Nazeeruddin, One-Year Stable Perovskite Solar Cells by 2D/3D Interface Engineering, *Nat. Commun.*, 2017, **8**, 15684.

3 G. Lozano, The Role of Metal Halide Perovskites in Next Generation Lighting Devices, *J. Phys. Chem. Lett.*, 2018, **9**, 3987–3997.

4 Z. Zhang, L. Ren, H. Yan, S. Guo, S. Wang, M. Wang and K. Jin, Bandgap Narrowing in Bi-Doped $CHNPbCl$ Perovskite Single Crystals and Thin Films, *J. Phys. Chem. C*, 2017, **121**, 17436–17441.

5 S. Kumavat, Y. Sonvane, D. Singh and S. Gupta, Two-Dimensional $CH_3NH_3PbI_3$ with High Efficiency and Superior Carrier Mobility: A Theoretical Study, *J. Phys. Chem. C*, 2019, **123**, 5231–5239.

6 H. Jung, C. Stompus, M. Kanatzidis and V. Dravid, Self-Passivation of 2D Ruddlesden–Popper Perovskite by Polytypic Surface PbI_2 Encapsulation, *Nano Lett.*, 2019, **19**, 6109–6117.

7 C. Motta, F. El-Mellouhi and S. Sanvito, Charge Carrier Mobility in Hybrid Halide Perovskite, *Sci. Rep.*, 2015, **5**, 12746.

8 G. Giorgi, J.-I. Fujisawa, H. Segawa and K. Yamashita, Small Photocarrier Effective Masses Featuring Ambipolar Transport in Methylammonium Lead Iodide Perovskite: A Density Functional Analysis, *J. Phys. Chem. Lett.*, 2013, **4**, 4213–4216.

9 A. Krishna, S. Gottis, M. Nazeeruddin and F. Sauvage, Mixed Dimensional 2D/3D Hybrid Perovskite Absorbers: The Future of Perovskite Solar Cells?, *Adv. Funct. Mater.*, 2018, 1806482.

10 A. Bala, A. Deb and V. Kumar, Atomic and electronic Structure of Two Dimensional Inorganic Halide perovskites $A_{n+1}M_nX_{3n+1}$ (n = 1–6, A = Cs, M = Pb and Sn, and X = Cl, Br, and I) from *Ab Initio* Calculations, *J. Phys. Chem. C*, 2018, **12**, 7464–7473.

11 D. O. Demchenko, N. Izyumskaya, M. Feneberg, V. Avrutin, U. Ozgur, R. Goldhahn and H. Morkoc, Optical Properties of the Organic-Inorganic Hybrid Perovskite $CH_3NH_3PbI_3$: Theory and Experiment, *Phys. Rev. B*, 2016, **94**, 075206.

12 A. Agresti, S. Pescetelli, A. L. Palma, A. Castillo, D. Konios, G. Kakavelakis, S. Razza, L. Cina, E. Kymakis, F. Bonaccorso and A. Carlo, Graphene Interface Engineering for Perovskite Solar Modulus: 12.6% Power Conversion Efficiency over 50 cm^2 active Area, *ACS Energy Lett.*, 2017, **2**, 279–287.

13 L. Zhang and W. Liang, How the Structures and Properties of Two-Dimensional Layered Perovskites $MAPbI_3$ and $CaPbI_3$ Vary with the Number Layers, *J. Phys. Chem. Lett.*, 2017, **8**, 1517–1523.

14 H. Tsai, W. Nie, J.-C. Blancon, C. C. Stoumpos, R. Asadpour, *et al.*, High-Efficiency Two-Dimensional Ruddlesden-Popper Perovskite Solar Cells, *Nature*, 2016, **536**, 312–316.

15 C. Stoumpos, D. Cao, D. Clark, J. Young, J. Rondinelli, J. Jang, J. Hupp and M. Kanatzidis, Ruddlesden-Popper Hybrid Lead Iodide Perovskite 2D homologus Semiconductors, *Chem. Mater.*, 2016, **28**, 2852–2867.

16 F. Corsini and G. Griffini, Recent progress in encapsulation strategies to enhance the stability of organometal halide perovskite solar cells, *J. Phys. Energy*, 2020, **2**, 031002.

17 X. Gao, X. Zhang, W. Yin, H. Wang, Y. Hu, Q. Zhang, Z. Shi, V. Colvin, W. Yu and Y. Zhang, Ruddlesden-Popper Perovskites: Synthesis and Optical Properties for Optoelectronic Applications, *Adv. Sci.*, 2019, **6**, 1900941.

18 M. E. Kamming, H.-H. Fang, M. A. Loi, G. Brink, G. Black, T. Palstra and J. Elshof, Micropatterned 2D Hybride Perovskite Thin Films with Enhanced Photoluminescence Lifetimes, *ACS Appl. Mater. Interfaces*, 2018, **10**, 12878–12885.

19 R. K. Misra, B. Cohen, L. Iagher and L. Etgar, Low Dimensional Organic–Inorganic Halide Perovskite: Structure, Properties, and Applications, *ChemSusChem*, 2017, **10**, 3712–3721.

20 J. Lu and Z. Wei, The Strategies for preparing blue perovskites light-emitting diodes, *J. Semicond.*, 2020, **41**, 051203.

21 X. Chin, D. Cortecchia, J. Yin, A. Bruno and C. Soci, Lead Iodide Perovskite Light-Emitting Filed Effect Transistor, *Nat. Commun.*, 2015, **6**, 7383.

22 Z. Wang, J. Liu, Z. Q. Xu, Y. Xue, L. Jiang, J. Song, F. Huang, Y. Wang, Y. L. Zhong, Y. Zhang, Y.-B. Cheng and Q. Bao, Wavelength-Tunable Waveguide Based on Polycrystalline Organic- Inorganic Perovskite Microwave, *Nanoscale*, 2016, **8**, 6258–6264.

23 E. J. Yoo, M. Lyu, J. H. Yun, C. J. Kang, Y. J. Choi and L. Wang, Resistive Switching Behavior in Organic-Inorganic Hybrid $CH_3NH_3PbI_{3-x}Cl_x$ Perovskite for Resistive Random Access Memory Devices, *Adv. Mater.*, 2015, **27**, 6170–6175.

24 G. Xing, N. Mathews, S. S. Lim, N. Yantara, X. Liu, D. Sabba, M. Gratzel, S. Mhaisalkar and T. C. Sum, Low-Temperature Solution Processed Wavelength-Tunable Perovskite for Lasing, *Nat. Mater.*, 2014, **13**, 476–480.

25 Y. Fang, Q. Dong, Y. Shao, Y. Yuan and J. Huang, Highly Narrowband Perovskite Single-crystal Photodetectors Enable by Surface-Charge Recombination, *Nat. Photonics*, 2015, **9**, 679–686.

26 G. Niu, W. Li, F. Meng, L. Wang, H. Dong and Y. Qiu, Study on the stability of $CH_3NH_3PbI_3$ films and the effect of post-modification by aluminum oxide in all-solid-state hybrid solar cells, *J. Mater. Chem. A*, 2014, **2**, 705–710.

27 I. C. Smith, E. Hoke, D. Solis-lbarra, M. McGehee and H. Karunadasa, A Layered Hybrid Perovskite Solar Cell Absorber with Enhanced Moisture Stability, *Angew. Chem., Int. Ed.*, 2014, **53**, 11232–11235.

28 Y. Zhou and Y. Zhao, Chemical stability and instability of inorganic halide perovskites, *Energy Environ. Sci.*, 2019, **12**, 1495–1511.

29 Z. Wang, Z. Shi, T. Li, Y. Chen and W. Huang, Stability of Perovskites Solar Cells: A Prospective on the Substitution of the A Cation and X Anion, *Angew. Chem., Int. Ed.*, 2017, **56**, 1190–1212.

30 D. Liang, Y. Peng, Y. Fu, M. J. Shearer, J. Zhang, J. Zhai, Y. Zhang, R. J. Hamers, T. L. Andrew and S. Jin, Colorpure violet-light-emitting diodes based on layered lead halide perovskite nanoplates, *ACS Nano*, 2016, **10**, 6897–6904.

31 F. Chiarella, A. Zappettini, F. Licci, I. Borriello, G. Cantele, D. Ninno, A. Cassinese and R. Vaglio, Combined experimental and theoretical investigation of optical, structural, and electronic properties of $CH_3NH_3SnX_3$ thin films (X = Cl, Br), *Phys. Rev. B: Condens. Matter Mater. Phys.*, 2008, **77**, 045129.

32 K. Yamada, K. Nakada, Y. Takeuchi, K. Nawa and Y. Yamane, Tunable Perovskite Semiconductor $CH_3NH_3SnX_3$ (X = Cl, Br, or I) Characterized by X-ray and DTA, *Bull. Chem. Soc. Jpn.*, 2011, **84**, 926–932.

33 F. Funabiki, Y. Toda and H. Hosono, Optical and Electrical Properties of Perovskites Variant $(CH_3NH_3)_2SnI_6$, *J. Phys. Chem. C*, 2018, **122**, 10749–10754.

34 K. Zheng and T. Pullerits, Two Dimensions Are Better for Perovskites, *J. Phys. Chem. Lett.*, 2019, **10**, 5881–5885.

35 C. Stoumpos, C. Soe, H. Tsai, W. Nie, J. Blancon, D. Cao, F. Liu, B. Traore, C. Katan, J. Even, A. Mohite and M. Kanatzidis, High Members of the 2D Ruddlesden-Popper Halide Perovskites: Synthesis, Optical Properties, and Solar Cells of $(CH_3(CH_2)_3NH_3)_2(CH_3NH_3)_4Pb_5I_{16}$, *Chem*, 2017, **2**, 427–440.

36 C. Underwood, J. Carey and S. Silva, Nonlinear Band Gap Dependence of Mixed Pb-Sn 2D Ruddlesden-Popper $PEA_2Pb_{1-x}Sn_xI_4$ Perovskites, *J. Phys. Chem. Lett.*, 2021, **12**, 1501–1506.

37 Y. Hua, Y. Zhou, D. Hong, S. Wan, X. Hu, D. Xie and Y. Tian, Identification of the Band Gap Energy of Two-dimensional $(OA)_2(MA)_{n-1}Pb_nI_{3n+1}$ Perovskite with up to 10 Layers, *J. Phys. Chem. Lett.*, 2019, **10**, 7025–7030.

38 R. Dong, C. Lan, X. Xu, X. Liang, X. Hu, D. Li, Z. Zhou, L. Shu, S. Yip, C. Li, *et al.*, Novel Series of Quasi-2D Ruddlesden-Popper Perovskites Based on Short-Chained Spacer Cation for Enhanced Photodetection, *ACS Appl. Mater. Interfaces*, 2018, **10**, 19019–19026.

39 X. Tian, Y. Zhang, R. Zheng, D. Wei and J. Liu, Two-dimensional Organic–inorganic Hybrid Ruddlesden–Popper Perovskite Materials: Preparation, Enhanced Stability, and Applications in Photodetection, *Sustainable Energy Fuels*, 2020, **4**, 2087–2113.

40 A. Z. Chen, M. Shiu, J. H. Ma, M. R. Alpert, D. Zhang, B. J. Foley, D.-M. Smilgies, S.-H. Lee and J. J. Choi, Origin of Vertical Orientation in Two-Dimensional Metal Halide Perovskite and Its Effect on Photovoltaic Performance, *Nat. Commun.*, 2018, **9**, 1336.

41 S. Kumavat, Y. Sonvane and S. Gupta, Structural, optical, transport, and solar cell properties of 2D halide perovskite $MAZX_3$ (Z = Pb, Sn, and X = Cl, Br, I), *J. Appl. Phys.*, 2020, **128**, 114304.

42 H. Zheng, G. Liu, L. Zhu, J. Ye, X. Zhang, A. Alsaedi, T. Hayat, X. Pan and S. Dai, The Effect of Hydrophobicity of Ammonium Salts on Stability of Quasi-2D Perovskite Materials in Moist Condition, *Adv. Energy Mater.*, 2018, **8**, 1800051.

43 H. Kagdada, S. Gupta, S. Sahoo and D. Singh, Rashba Splitting in Two Dimensional Hybrid Perovskite Materials for High Efficient Solar and Heat Energy Harvesting, *J. Phys. Chem. Lett.*, 2020, **11**, 7679–7686.

44 J.-H. Yang, Q. Yuan and I. Yakobson, Chemical Trends of Electronic Properties of Two-Dimensional Halide Perovskite and Their Potential Application for Electronic and Optoelectronics, *J. Phys. Chem. C*, 2016, **120**, 24682–24687.

45 J.-H. Yang, Q. Yuan and I. Yakobson, Chemical Trends of Electronic Properties of Two-Dimensional Halide Perovskite and Their Potential Application for Electronic and Optoelectronics, *J. Phys. Chem. C*, 2016, **120**, 24682–24687.

46 W. E. I. Sha, X. Ren, L. Chen and W. C. H. Choy, The Efficiency Limit of $CH_3NH_3PbI_3$ Perovskite Solar Cells, *Appl. Phys. Lett.*, 2015, **106**, 221104.

47 C. Lopez, C. Abia, J. Gainza, P. Kayser, N. Nemes, O. Dura, J. Martinez, M. Fernandez-Diaz, C. Alvarez-Galvan and J. Alonso, Structural evolution, optical gap and thermoelectric properties of $CH_3NH_3SnBr_3$ hybrid perovskite, prepared by mechanochemistry, *Mater. Adv.*, 2021, **2**, 3620.

48 R. Chakraborty and A. Nag, Correlation of Dielectric Confinement and Excitonic Binding Energy in 2D Layered Hybrid Perovskites Using Temperature Dependent Photoluminescence, *J. Phys. Chem. C*, 2020, **124**, 16177–16185.

49 F. Hao, C. C. Stoumpos, D. H. Cao, R. P. H. Chang and M. G. Kanatzidis, Lead free solid-state organic-inorganic halide perovskite solar cells, *Nat. Photonics*, 2014, **8**, 489–494.

50 Q. Sun and W. Yin, Thermodynamic Stability Trend of Cubic Perovskites, *J. Am. Chem. Soc.*, 2017, **139**, 14905–14908.

51 H. Xu, H. Yuan, J. Duan, Y. Zhao, Z. Jiao and Q. Tang, Lead-free $CH_3NH_3SnBr_{3-x}I_x$ perovskite quantum dots for mesoscopic solar cell applications, *Electrochim. Acta*, 2018, **282**, 807–812.

52 A. Shukla, V. Sharma, S. Gupta and A. Verma, Computational determination of the physical thermoelectric parameter of tin based organometallic halide perovskites ($CH_3NH_3SnX_3$

X= Br and I): Emerging materials for optoelectronic devices, *Mater. Chem. Phys.*, 2020, **253**, 123389.

53 N. Zibouche and M. S. Islam, Structure–Electronic Property Relationships of 2D Ruddlesden–Popper Tin- and Lead-based Iodide Perovskites, *ACS Appl. Mater. Interfaces*, 2020, **12**, 15328–15337.

54 K. Korshunova, L. Winterfeld, W. Beenken and E. Runge, Thermodynamic stability of mixed Pb:Sn methyl-ammonium halide perovskites, *Phys. Status Solidi B*, 2016, **253**, 1907–1915.

55 K. Amnuyswat and P. Thanomngam, Roles of spin-orbit coupling in tetragonal hybrid halide perovskite for photovoltaics light-absorber, *Mater. Today: Proc.*, 2018, **5**, 14857–14861.

56 Z. Wang, F. Wang, B. Zhao, S. Qu, T. Hayat, A. Alsaedi, L. Sui, K. Yuan, J. Zhang, Z. Wei and Z. Tan, Efficient Two-Dimensional Tin Halide Perovskite Light-Emitting Diodes *via* a Spacer Cation Substitution Strategy, *J. Phys. Chem. Lett.*, 2020, **11**, 1120–1127.

57 A. Iefanova, N. Adhikari, A. Dubey, D. Khatiwada and Q. Qiaoa, Lead free $CH_3NH_3SnI_3$ perovskite thin-film with p-type semiconducting nature and metal-like conductivity, *AIP Adv.*, 2016, **6**, 085312.

58 E. McClure, A. McCormick and P. Woodward, Four Lead-free Layered Double Perovskites with the n =1 Ruddlesden–Popper Structure, *ACS Inorg. Chem.*, 2020, **59**, 6010–6017.

59 L. Ma, M. Ju, J. Daia and X. Zeng, Tin and Germanium Based Two-dimensional Ruddlesden–Popper Hybrid Perovskites for Potential Lead-Free Photovoltaic and Photoelectronic Applications, *Nanoscale*, 2018, **10**, 11314–11319.

60 S. Ghosh, D. D. Sante and A. Stroppa, Strain Tuning of Ferroelectric Polarization in Hybrid Organic Inorganic Perovskite Compounds, *J. Phys. Chem. Lett.*, 2015, **6**, 4553–4559.

61 M. D. Ventra and S. T. Pantelides, Hellmann-Feynman Theorem and the Definition of Force in Quantum Time-Dependent and Transport Problems, *Phys. Rev. B: Condens. Matter Mater. Phys.*, 2000, **61**, 16207.

62 M. Baranowski, S. J. Zelewski, M. Kepenekian, B. Traoré, J. M. Urban, A. Surrente, K. Galkowski, D. K. Maude, A. Kuc, E. Booker, R. Kudrawiec, S. D. Stranks and P. Plochocka, Phase-Transition-Induced Carrier Mass Enhancement in 2D Ruddlesden–Popper Perovskites, *ACS Energy Lett.*, 2019, **4**, 2386–2392.

63 P. Blöchl, Projected Augmented-Wave Method, *Phys. Rev. B: Condens. Matter Mater. Phys.*, 1994, **50**, 17953.

64 G. Kresse and J. Furthermullaer, Efficient Iterative Schemes for *ab initio* Total Energy Calculations Using a Plane-Wave Basis Set, *Phys. Rev. B: Condens. Matter Mater. Phys.*, 1996, **54**, 11169.

65 G. Kresse and D. Joubert, From Ultrasoft Pseudopotentials to the Projected Augmented-Wave Method, *Phys. Rev. B: Condens. Matter Mater. Phys.*, 1999, **59**, 1758.

66 J. Perdew, K. Burke and M. Ernzerhof, Generalized Gradient Approximation Made Simple, *Phys. Rev. Lett.*, 1997, **78**, 1396.

67 J. Heyd, G. E. Scuseria and M. Ernzerhof, Hybrid Functionals Based on Screened Coulomb Potential, *J. Chem. Phys.*, 2003, **118**, 8207–8215.

68 Y. Yamada, T. N. M. Endo, A. Wakamiya, Y. Kanemitsu, *et al.*, Photo Carrier Recombination Dynamics in Perovskite $CH_3NH_3PbI_3$ for Solar Cell Applications, *J. Am. Chem. Soc.*, 2014, **136**, 11610–11613.

69 W.-J. Yin, J.-H. Yang, J. Kang, Y. Yan and S.-H. Wei, Halide Perovskite Materials for Solar Cells: a Theoretical Review, *J. Mater. Chem. A*, 2015, **3**, 8926–8942.

70 B. W. Veal and A. P. Paulikas, Optical Properties of Molybdenum. I. Experiment and Kramers-Kronig Analysis, *Phys. Rev. B: Solid State*, 1974, **10**, 1280.

71 M. Dressel and M. Scheffler, Verifying the Drude Response, *Ann. Phys.*, 2006, **15**, 535–544.